

# Chirality induced phase separation in active circle swimmers

Divya Kushwaha\* and Shradha Mishra†  
Indian Institute of Technology (BHU) Varanasi, India 221005

(Dated: October 23, 2024)

Many microswimmers are inherently chiral, and this chirality can introduce fascinating behaviors in a collection of microswimmers. The dynamics become even more intriguing when two types of microswimmers with distinct chirality are mixed. Our study considers a mixture of self-propelled particles with opposite chirality, examining how the system's characteristics evolve as the magnitude of chirality is tuned. In weakly chiral systems, the particles exhibit similar behavior, leading to a globally flocking phase where both types of particles are well-mixed. However, in an intermediate range of chirality, the particles demix and follow their trajectories, creating a competition between chirality and self-propulsion. This competition results in interesting phases within the system. We explore the characteristics of these different phases in detail, focusing on the roles of self-propulsion speed and chirality.

## I. INTRODUCTION

Active matter is a fascinating area of study [1–5] that focuses on self-propelled entities such as active colloids [6], insects swarm in large groups [7], fish display schooling in the ocean [8], and birds flock in the sky [9], groups of animals at the macroscopic scale [10], *etc.* These entities move due to internal mechanisms such as chemical reactions, cilia, flagella, and internal motors utilizing the input from the surrounding mediums. Understanding collective behavior in active matter is crucial for uncovering the interpretation of collective behavior. Flocking, which refers to the collective motion of organisms, is also observed in inanimate macroscopic systems, such as active granular rods [11]. This widespread phenomenon often involves transitions from disordered to long-range ordered states, influenced by factors like density and noise [12].

The dynamics of active agents can be categorized into two main types: one involves nearly straight movement with random directional changes, creating a sense of self-propulsion without any perception of rotation, as seen in active colloids like Janus particles, molecular motors [13], natural low-Reynolds-number swimmers [14–16], active particles on periodic lattice [17] and polar active granular particles [18]. The second type is characterized by particles, which have a sense of rotation or chiral particles. Systematically, particles can tend to rotate clockwise or anticlockwise. The motion is circular in two dimensions and helical in three dimensions [19, 20]. These chiral particles possess a characteristic self-propulsion velocity and a chirality that determines the rate of directional change in the absence of fluctuations. The radius of their trajectories is determined by the ratio of the self-propulsion

velocity to the chirality. This type of chiral motion is observed in various systems, including biological circle swimmers like bacteria [21], E.coli [22, 23], sperm cells [24, 25], L-shape artificial microswimmers [26] and magnetotactic bacteria in rotating external fields [27, 28].

While most research on bacterial swarming and collective swimming has concentrated on homogeneous systems [29–32], which involve agents having identical features. The natural world notably encounters mixtures of particles of different chiralities [33, 34]. These differences arise from variations in their size [35], diverse orientations, and mixed-species behavior [36, 37]. Complex systems are inherently heterogeneous, as individuals differ in their properties, responses to the environment, and interactions. The collective motion of such heterogeneous systems has been extensively studied, revealing complexities other than those observed in homogeneous systems. Some significant studies have delved into macroscopic colony growth and spatial mixing between populations [38–43].

In this study, we investigate an inhomogeneous system focusing on the collective dynamics of a mixed binary mixture of self-propelled particles with different chiralities. We introduce two types of chiral particles, each constituting half of the total population, with one group exhibiting clockwise (*CW*) rotational tendency and the other anticlockwise (*ACW*) tendency. This inherent rotation creates heterogeneity within the system. Our primary aim is to understand how these particles interact when they encounter those with particles of opposite nature, particularly under varying parameters *like*: self-propulsion speed ( $v_0$ ) and chirality ( $\Omega$ ). At low  $\Omega$ , the system shows mixed flocking behavior where particles exhibit only slight rotational tendencies. As  $\Omega$  increases, *CW* and *ACW* particles begin to separate, forming dense clusters aligned with their rotational directions, resulting in two distinct clusters at moderate

\* divyakushwaha.rs.phy22@itbhu.ac.in

† smishra.phy@itbhu.ac.in

$\Omega$  values. Interestingly, at large chirality, particles remain homogeneously mixed at low self-propulsion speeds ( $v_0 = 0.001$ ), rotating uniformly on their axes rather than separating. This phenomenon occurs because as  $\Omega$  increases, particles show biased behavior based on their orientation, positive and negative chiral particles tend to move in *CW* and *ACW* trajectories, but the self-propulsion speed is not strong enough to separate them. The kinetics of phase separation shows the algebraic growth with growth exponent  $1/4$ , the same as for other active systems [44, 45]. This study highlights the intricate interplay between self-propulsion speed and rotational bias due to chirality, revealing various complex behaviors in chiral active systems.

The rest of the article is structured as follows: Section II introduces the model for the dual chiral active particles system. The results and discussion of our system are detailed in Section III. Section III B explores the dynamic phases of particles. Finally, Section IV contains the discussion of our results and conclusions.

## II. MODEL AND NUMERICAL DETAILS

Our system comprises two types of chiral particles, each containing an equal number of  $N_1 = N_2 = N/2$  particles. These particles possess the same magnitude of chirality with opposite signs. They are distributed across a two-dimensional, off-lattice plane within an  $L \times L$  square box with periodic boundaries. The particles are represented as point particles and interact within a defined radius denoted as  $R$ . Initially, these particles are randomly dispersed in terms of both position  $\mathbf{r}_i$  and direction ( $\theta_i$  ranging from  $[-\pi, \pi]$ ), each having a constant self-propelled speed  $v_0$ . The temporal update of positional and direction is done at an interval of  $\Delta t$ . The particle's position is updated as follows:

$$\mathbf{r}_i(t + \Delta t) = \mathbf{r}_i(t) + \mathbf{v}_i(t)\Delta t \quad (1)$$

In the given equation,  $\mathbf{r}_i(t)$  denote the positions of the  $i^{\text{th}}$  particle at time  $t$ , where  $i$  can run from  $i = 1, 2, \dots, N$ .  $\mathbf{v}_i(t) \equiv (v_0 \cos(\theta_i), v_0 \sin(\theta_i))$ , represents the velocity of  $i^{\text{th}}$  particle at time  $t$ . Here,  $\theta_i(t)$  is its orientation and each particle has a constant velocity magnitude  $v_0$ . The particles interact locally within their interaction radius  $R$  as shown in Fig.1. To incorporate the chiral nature of the particles, the direction of the  $i^{\text{th}}$  particle is updated according to:

$$\theta_i(t + \Delta t) = \langle \theta_j(t) \rangle_{iR} + \Omega \Delta t + \Delta \theta \quad (2)$$

The  $\langle \theta_j(t) \rangle_{iR}$  represents the average of the directions of all the  $j$  particles within a defined interaction radius  $R$  of the  $i^{\text{th}}$  particle. This average direction is calculated

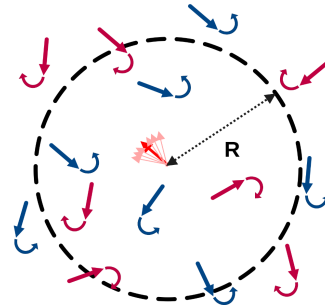


FIG. 1. (color online) A schematic representation of the model showing two types of chiral particles with their orientation directions: red for  $\Omega^+$  (clockwise rotation, *CW*) and blue for  $\Omega^-$  (anticlockwise rotation, *ACW*). The red arrow in the center of the dashed circle is the  $i^{\text{th}}$  particle and the dotted line represents the radius of the interaction range  $R$ . The light red arrows show the effect of random noise  $\Delta\theta$ . The curved arrows with each particle represent the chiral nature of particles.

by considering the orientations of all particles within this interaction radius. Mathematically, it is expressed as:

$$\langle \theta_j(t) \rangle_{iR} = \tan^{-1} \left[ \frac{\langle \sin \theta_j(t) \rangle_{iR}}{\langle \cos \theta_j(t) \rangle_{iR}} \right]$$

In this context,  $\langle \sin \theta_j(t) \rangle_{iR}$  and  $\langle \cos \theta_j(t) \rangle_{iR}$  denote the average values of  $\sin \theta$  and  $\cos \theta$ , respectively, for all particles within the interaction radius  $R$  of the  $i^{\text{th}}$  particle. Chirality is introduced using the parameter  $\Omega$ , where a positive value (denoted as  $\Omega^+$ ) signifies *CW* rotation and a negative value (denoted as  $\Omega^-$ ) represents *ACW* rotation. The magnitude of the chirality is given by  $|\Omega^\pm| = \Omega$ .  $\Delta\theta$  represents the angular noise, which is modeled as  $\Delta\theta = \eta \xi_i(t)$ ,  $\eta$  represents the noise amplitude and  $\xi(t)$  is random variable with zero mean  $\langle \xi_i(t) \rangle = 0$ , delta correlated  $\langle \xi_i(t_1) \xi_j(t_2) \rangle = \delta_{ij} \delta(t_1 - t_2)$  and uniformly distributed in  $[-\pi, \pi]$ . This directional update ensures that the particles demonstrate chiral behavior while considering the average direction of their neighbors within the interaction radius. The noise strength  $\eta$  is set to 0.2, so the system is in the ordered state for a zero-chirality  $\Omega = 0.0$ . The time difference for updating particles position and orientation is fixed to  $\Delta t = 1.0$ . The system is studied for  $v_0 \in (0.001, 0.5)$  and  $\Omega \in (0.001, 0.5)$ . Additionally, the interaction radius is fixed at  $R = 1$ , and the total particle density is maintained at  $\rho = \frac{N}{L^2} = 1.0$  ( $N = 1600 - 10000, L = 40 - 100$ ), with *CW* and *ACW* particles each having density 0.5. We let the system evolve, starting with the random homogeneous mixed state of both types of particles, and the position and orientation of particles are updated using Eqs. (1), (2). One simulation step is counted once all the  $N$  particles, positions and orientations are updated once. The kinetics of the system is studied for total  $t = 2^{16}$  time steps

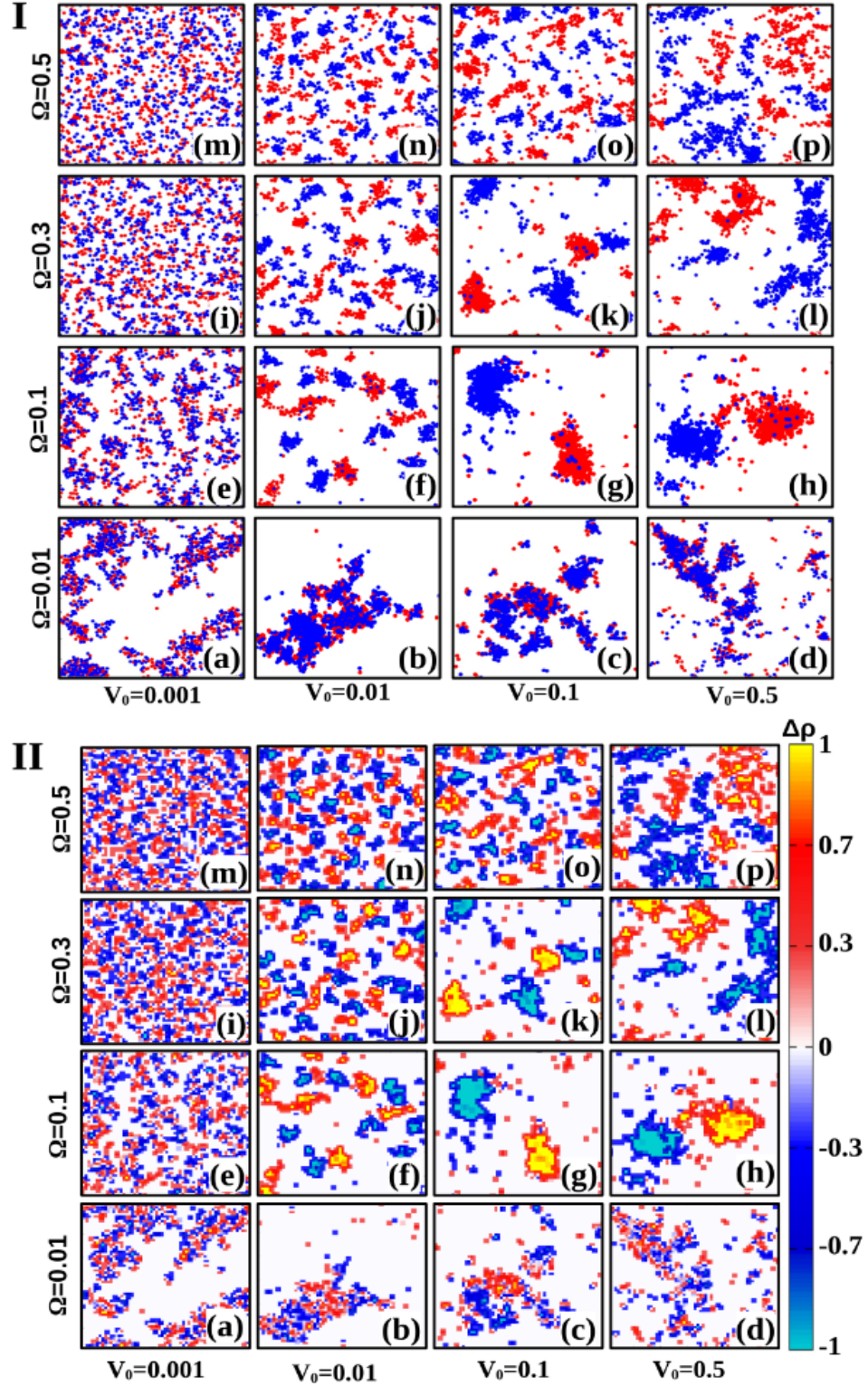


FIG. 2. (color online) (I) The figure illustrates the snapshots of the system for  $L = 40$  and at time  $t = 2^{17}$ . The red dots correspond to particles with positive chirality, denoted by  $\Omega^+$  and the blue dots represent particles with negative chirality  $\Omega^-$ . These particles are distributed across the coordinate plane, visualizing their spatial arrangement within the system. (II) This figure shows the density difference  $\Delta\rho$  for the same system parameters as for (I). The color map indicates the range of  $\Delta\rho$ : blue regions where  $\rho^-$  exceeds, red regions where  $\rho^+$  dominates, and white regions are empty regions. Both panels are depicted in the parameter space of chirality  $\Omega$ , varying from 0.01 to 0.5, and self-propulsion velocity  $v_0$ , ranging from 0.001 to 0.5.

and steady-state results are obtained by total simulation steps of  $2^{17}$ , with time average over the last  $2^{15} - 2^{17}$  times steps. Further, the averaging of data for the kinetics of the system is performed over 200–500 independent realizations and the steady state results are obtained by doing the ensemble averaging of data over 10 independent realizations.

### III. RESULTS AND DISCUSSION

Our study focuses on two distinct parameters: the self-propulsion speed ( $v_0$ ) and the magnitude of chirality ( $\Omega$ ). By systematically varying these parameters, we can observe the emergence of various phases within the system characterized by fixed noise ( $\eta$ ) and density ( $\rho$ ).

#### A. Steady state characteristics

We first show the snapshots of the system in the steady state at time  $t = 2^{17}$ . In Fig. 2(I) we show the location of two types of particles with two different colors (the red and blue colors represent the *CW* and *ACW* particles respectively) and Fig. 2(II) shows the local density difference between two types of particles. The local density of both types of particles  $\rho^\pm(\mathbf{r})$  in the system is obtained by dividing the whole system into coarse-grained square cells of size  $0.625 \times 0.625$  and counting the density of particles in each cell centered around point  $\mathbf{r}$  in the system. Further, the normalized density difference of two types of particles is defined as  $\Delta\rho(\mathbf{r}) = \frac{\rho^+(\mathbf{r}) - \rho^-(\mathbf{r})}{\rho^+(\mathbf{r}) + \rho^-(\mathbf{r})}$ . In Figs. 2(II) we show the snapshots of the system, for the density difference  $\Delta\rho(\mathbf{r})$  shown in the color bar. The white regions in Fig. 2(II) represent the empty regions. The *+ve* and *-ve* values of  $\Delta\rho$  indicate the majority of particles are of *CW* and *ACW* in nature, respectively. In Fig. 3 we show the orientation  $\theta_i \in (-\pi, \pi)$  of particles at the same time as for Fig. 2. Now we will explain our observations from Fig. 2(I-II) and 3.

In the lower chirality regime  $\Omega = 0.01$ , the particles remain mixed irrespective of their speed as is evident from the density snapshots in Fig.2II(a-d) and the particle snapshots in Fig.2(I)(a-d). However, there is a change in global alignment among the particles in each participating cluster, as the self-propulsion velocity is tuned. For smaller magnitudes of self-propulsion, the particles tend to rotate about their own axis before they go beyond their interaction region and this hinders their chance to interact with new neighbors and system remains nearly homogeneous and weak orientational or-

dering, as can be seen by the presence of multiple colors<sup>4</sup> in the orientation plot for small  $v_0 = 0.001$  and  $0.01$  in Figs.3(a,b). However as  $v_0$  is increased, self-propulsion dominates over the rotation due to chirality, in turn enhancing interaction between particles, thus giving rise to a global alignment in the system. This is represented by a color in the majority for higher values of  $v_0 = 0.1$  and  $0.5$  as shown in Fig.3(c-d). But all through this, the lower magnitude in chirality results in very little orientational difference between both the nature of particles and proves to be insufficient to segregate them ultimately giving rise to a mixed phase. The mixed nature of both the particle types can be seen by the mixing up of colors in Fig. 2(I)(c-d) and small density differences  $\Delta\rho$  in Fig.2(II)(c-d).

As we subject the system to a slightly higher chirality we observe varying behaviors based on the magnitude of self-propulsion. Now, as the chirality is higher it dominates over  $v_0$  for lower self-propulsion values. The particles are then devoid of any chances to interact with each other and mostly rotate in small circles and hence remain in a mixed state, also reducing the global ordering in the process. This can be seen in Fig.2(I-II)(e) and Fig.3(e). On increasing  $v_0$ , we see that the particles start forming small rotating clusters (as seen in Fig.2(I)(f)) and each cluster has its own local ordering. This is because the chirality is strong enough to create small pockets of rotating clusters and the self-propulsion causes the particles to separate from each other. On further increase in self-propulsion, the particles traverse larger steps before eventually deflecting from their trajectory. But the curvature is strong enough to get the particles separated from each other very soon. Subsequently, it is seen that continuing to increase self-propulsion promotes phase separation and ultimately a global phase-separated state appears for a large  $v_0 = 0.5$  containing two distinct clusters of two types of particles.

Now as we go to even higher chirality(0.3), smaller regimes of self-propulsion expectedly give rise to mixed phases, as rotational tendencies of the particles dominate over their self-propulsion. On increasing self-propulsion we see particles are grouping to form small clusters with local cluster alignment similar to the case discussed previously. However, on continuing to increase self-propulsion there is a subtle difference from the previously discussed case of chirality with high self-propulsion. Now the cumulative effects of comparatively higher chirality and self-propulsion  $v_0$  enhance the translational motion of the particles and deflect their trajectories, weakening the orientation interaction, in the process, resulting in a reduced density within the cluster (as shown in Fig.2II(l)). However, the chirality



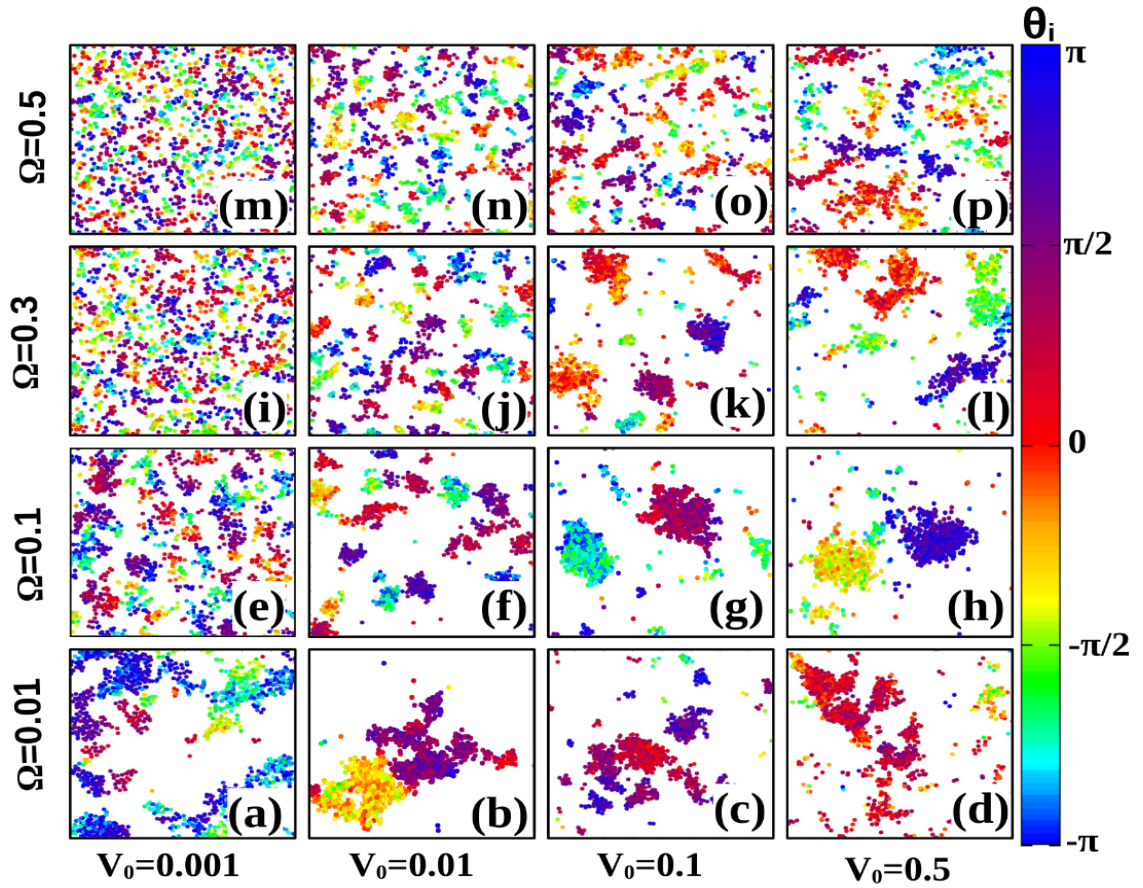


FIG. 3. (color online) Shows the snapshots for the orientation of particles. In this figure, the color represents the direction of particles  $\theta_i$  for different  $\Omega$  and  $v_0$ . The parameters are the same as in Fig. 2(I)

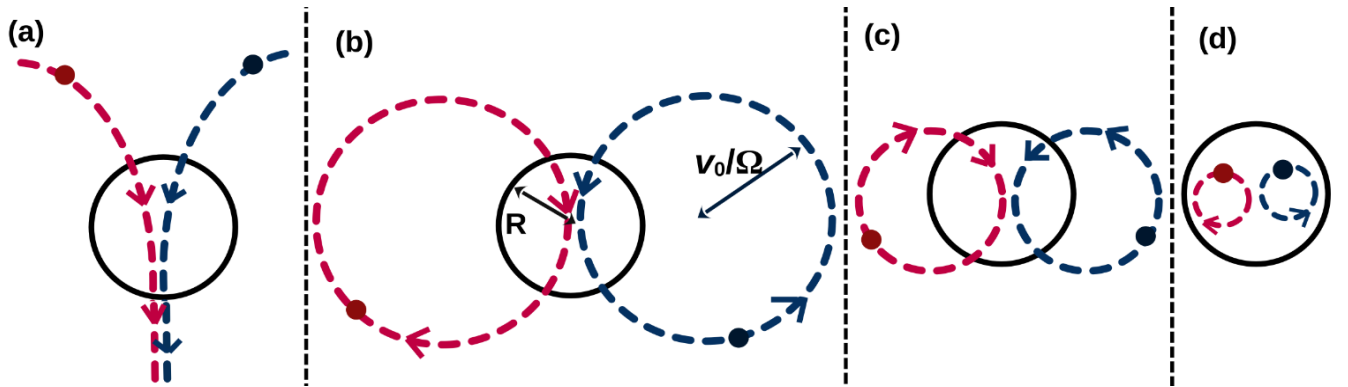


FIG. 4. The figures (a), (b), (c) and (d) depict the cartoon of the trajectories of one *CW* (red) and one *ACW* (blue) chiral active particles. The solid black circle represents the interaction range with a radius  $R = 1$ , within which the chiral particles interact with each other. The dashed lines show the cartoon of the trajectories of two types of particles with arrows on them representing the directions of velocity of particles. The dots on the dashed line is the location of two types of particles at some arbitrary time. (a)  $v_0 = 0.5$  and  $\Omega = 0.01$ , the radius of the chiral particle trajectory ( $r_0 = \frac{v_0}{\Omega} = 50$ ) is significantly larger than the interaction range. (b)  $v_0 = 0.5$  and  $\Omega = 0.1$ , the trajectories are comparable in size to the interaction radius, resulting in the radius of the trajectory ( $r_0 = \frac{v_0}{\Omega} = 5$ ). (c)  $v_0 = 0.5$  and  $\Omega = 0.5$ , the radius of trajectory  $r_0 = \frac{v_0}{\Omega} = 1$  is nearly equal to the interaction radius. (d)  $v_0 = 0.2$  and  $\Omega = 0.5$ , the particle trajectories have a smaller radius  $r_0 = \frac{v_0}{\Omega} = 0.4$  than the interaction radius.

keeps the particles to be in a phase-separated state and maintains a common orientation with their neighbors as shown in Fig.3(l). As we continue to increase chirality to a value of 0.5 particles exhibit mixed phases (as seen in Fig.2(I-II)(m) and Fig.3(m)) similar to the previously discussed cases for low self-propulsion velocities. Here on increasing self-propulsion, although the particles form local clusters, their enhanced intrinsic rotational dynamics destroy the overall ordering within the cluster in turn weakening their phase transition and ultimately leading to dilute and expanded clusters (as seen in Fig.2(I-II)(n-p) and Fig.3(n-p)). Based on the range of chirality  $\Omega$  and activity  $v_0$  we characterize the four cases in the system. We can define the ratio  $r_0 = \frac{v_0}{\Omega}$  as the radius of the trajectory of a single particle at the mean-field level. Hence the ratio determines the curvature of the particle trajectory. Large ratio  $r_0$  means nearly straight line motion and small  $r_0$  means a particle rotating about its own axis. The ratio  $r_0$  can be compared to the one relevant length scale in the system: the interaction range  $R$ . Based on this comparison we can define the four scenarios in the parameter space.

*Case I:  $r_0 \gg R$ :* In this case, particle trajectory is nearly a straight line within the range of its interaction radius, and two types of particles may not experience their chirality and for large  $v_0$ , they will remain mixed and try to move in the same direction (flocking) and global mixed ordered state will develop in the system. This is the situation for  $(v_0, \Omega) = (0.1 - 0.5, 0.01)$  as can be seen in Fig. 2(I-II)(c-d) and 3(c-d). The cartoon of the trajectory of two types of particles is shown in Fig. 4(a).

*Case II:  $r_0 \geq R$ :* In this case, although particles maintain nearly the same orientation when lying within the interaction radius, very soon their trajectory gets deflected, they start moving in opposite directions and they leave the periphery of their previous neighbors and meet with other sets of neighbors. If the new neighbors have the same chirality, the particles will continue moving in the same direction. If not, their paths will be deflected again, leading them to a new location. This search will end with a state, where the majority of particles in the neighborhood are of similar chirality. Hence particles will phase separate, based on their chirality and macroscopic phase separation develops in the system. Each phase-separated cluster maintains ordering within the cluster as can be seen by Fig. 2(I-II)(g-h, l) and 3(g-h, l). The cartoon of the two particles' trajectory and their interaction is shown in Fig. 4(b).

*Case III  $r_0 \simeq R$ :* In this case, the particle's trajectory has larger curvature, and as soon as they leave the interaction radius they get separated from each other. But

since the radius of trajectory is of the order of interaction radius, hence small pockets of clusters develop and microscopic clustering is obtained in the system. The mechanism of microscopic clustering is the same as explained in *Case II* with a key difference that now particles can only go to the distance smaller than that in *Case II*, this leads to the formation of small clusters, as can be seen by Fig. 2(I-II)(f, j) and 3(f, j). The cartoon of the trajectory of the two particles and their interaction is shown in Fig. 4(c).

*Case IV:  $r_0 \ll R$ :* In this situation, particles do not get a chance to align and chiral nature dominates they keep rotating about their own axis and do not leave their interaction radius and hence remain mixed. as can be seen by Fig. 2(I-II)(i, m-n) and 3(i, m-n). The cartoon of the same is shown in Fig. 4(d). Till now we have discussed the characteristics of the system based on the snapshots, now we quantify the system behavior in the steady state by measuring the two order parameters, representing the phase separation and global orientation ordering. To explain the observed patterns as discussed before, we use the Phase separation order parameter (*PSOP*) ( $\Lambda$ ) to quantify the degree of mixing and demixing in the system and the Global order parameter (*GOP*) ( $\Phi$ ) to quantify the overall order and disorder within the system.

The PSOP is defined as:

$$\Lambda(t) = \frac{|n(\Omega^+, t) - n(\Omega^-, t)|}{n(\Omega^+, t) + n(\Omega^-, t)}$$

where  $n(\Omega^+, t)$  and  $n(\Omega^-, t)$  represent the number of particles with positive and negative chirality, respectively at time  $t$ , within the distance  $L/4$  (to differentiate the macroscopic phase separation in the system, We also checked for other distances,  $L/16$ ,  $L/8$ , etc., the behaviour of  $\Lambda$  remains the same.) Further, we take the mean of  $\Lambda(t)$  over the steady state when the  $\Lambda(t)$  remains statistically similar with respect to time. The mean is calculated over time in the steady state and over 10 independent realizations.

To further quantify the clustering and phase separation among the particles, we can also use the local density difference of two types of particles as defined before and shown in Fig. 2(II). Here we use the local density different  $\Delta\rho(\mathbf{r}, t)$  at different times in the steady state. Using the local density different  $\Delta\rho(\mathbf{r}, t)$  we calculated the two-point normalized correlation function  $C(r, t) = \langle \Delta\rho(\mathbf{r}_0, t)\Delta\rho(\mathbf{r} + \mathbf{r}_0, t) \rangle$ , where mean is over all the points  $\mathbf{r}_0$ , directions, different times in the steady state and over 10 ensembles. In the steady state the correlation function  $C(r, t)$  will depend on the two parameters  $v_0$  and  $\Omega$ . We further define the correlation length  $\mathcal{L}(v_0, \Omega, t)$  from the distance at which the correlation function reaches 10% of its value from the first data. In Fig. 5(a-b) we show the plot of *PSOP* and  $\frac{\mathcal{L}(v_0, \Omega)}{L/4}$  vs.

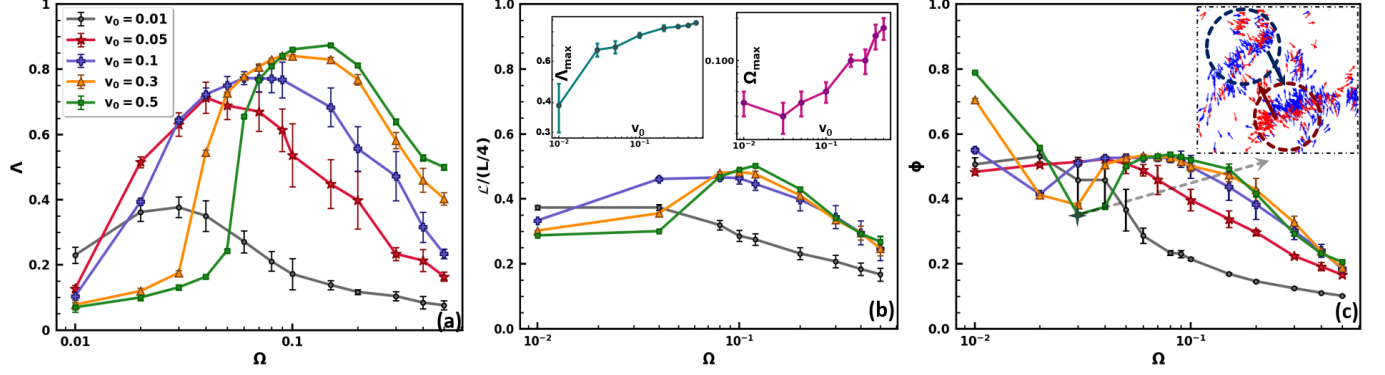


FIG. 5. (color online) (a) The  $\Lambda$  vs.  $\Omega$  for different  $v_0$ . (b) Correlation Length  $\mathcal{L}$  vs.  $\Omega$  for different  $v_0$ . Insets (I)  $\Lambda_{max}$  vs.  $v_0$  and  $\Omega_{max}$  vs.  $v_0$ . (c) The  $\Phi$  vs.  $\Omega$  for different  $v_0$ . The snapshot in the corner illustrates the mechanism of mixing which leads to a dip in  $\Phi$ . The snapshot is for  $v_0 = 0.5$  and  $\Omega = 0.05$  marked by *plus* in the figure. Two highlighted dotted circles (blue/red) show the dominance of  $-ve$  and  $+ve$  chiral particles. The small arrows show the direction of orientation of particles and the thick arrows show the local mean orientation of particles in each circle. The other parameters are the same as in Fig. 2(I).

$\Omega$  for different  $v_0 \in (0.01, 0.5)$  respectively. Very clearly both show the non-monotonic trend as a function of chirality. For small activity  $v_0 = 0.01$ , particles have very weak self-propulsion speed and for any finite chirality, the rotational nature dominates, and both  $PSOP$  and  $\mathcal{L}(v_0, \Omega)$  remain low with a small peak at  $\Omega \simeq 0.02$ . For very high  $\Omega$ , particles mainly remain stuck to their location and perform the circular motion. Hence do not get the chance to move out and phase separate. For moderate  $\Omega$ 's close to 0.02, chirality and activity are in comparison and they have some tendency to form small clusters. On increasing activity, initially, the  $PSOP$  and length  $\mathcal{L}$  increases, and then again for larger chirality it shows the monotonic decay to small values. The  $PSOP$  and  $\mathcal{L}$  show the gradual increment on the increasing  $v_0$  it reaches a maximum at  $\Omega_{max}(v_0)$ . The  $\Omega_{max}$  shifts towards the larger  $\Omega$  on increasing  $v_0$ , although the shift is weak as shown in Fig. 5(b) (inset II). For activity ranging from medium to high ( $v_0 > 0.05$ ), increasing the angular velocity  $\Omega$  keeps the system mixed for very small  $\Omega$ , and both the  $\Lambda$  and  $\mathcal{L}$  are low, indicating a lack of phase separation. As the angular velocity  $\Omega$  continues to increase, there is a bias in particle orientation, leading to an increase in phase separation. Consequently, the  $\Lambda$  and  $\mathcal{L}$  increase as the system and reaches to a maximum at  $\Omega_{max}$  and maximum phase separation occurs with particles of different chiralities segregating into dense clusters, as depicted in Fig.2(I-II)(g-h, l). However, as  $\Omega$  continue to increase, then beyond  $\Omega_{max}$  particles do get separated, but their trajectory is small and they are separated in a sparser form, causing the  $\Lambda$  and  $\mathcal{L}$  to decrease gradually. Also, increasing activity  $v_0$  leads to an increase in the phase separation as can be seen by the maximum value of  $\Lambda_{max}$  increases with  $v_0$ . The plot of  $\Lambda_{max}$  vs.  $v_0$  is shown in Fig. 5(inset I). For lower

values of  $v_0$   $v_0 \leq 0.05$ , the system does not exhibit a phase-separated state, rather multiple small clusters are formed as can be seen by snapshots Fig. 2(I-II)(f, j) the small length  $\Lambda$  and  $\mathcal{L}$  values in Fig. 5(a-b). Consequently, the  $\Lambda$  ( $\mathcal{L}$ ) does not increase significantly as it does for higher  $v_0$  values.

We also examine the Global Order Parameter ( $\Phi$ ) to understand the nature of the orientational ordering in our system. The  $\Phi$  is determined by calculating the absolute value of the average normalized velocity of all the particles in the system:

$$\Phi(t) = \frac{1}{Nv_0} \left| \sum_{i=1}^N v_i(t) \right|$$

Further the  $\Phi(t)$  is averaged over the times in the steady state and ensembles to get the mean order parameter  $\Phi$ . The  $\Phi$  is approximately equal to one when all particles move coherently in the same direction, indicating a highly ordered state. Conversely, the  $\Phi$  approaches zero when the motion of individual particles is random, reflecting a disordered state.

For activities in the medium to high range ( $v_0 \geq 0.1$ ), the global order parameter ( $\Phi$ ) initially decreases from its maximum value as shown in Fig.5(c). At low values of  $\Omega$ , the  $\Phi$  is at its peak because particles exhibit a low tendency to rotate and remain mixed and move in the same direction. Demixing creates the deflection in their trajectory and decreases in  $\Phi$ . The  $\Phi$  also increases as  $v_0$  increases while  $\Omega$  remains low. This can be observed in the orientation snapshots of particles in Fig. 3(c-d), which shows that at  $\Omega = 0.01$ , as  $v_0$  increases, there is a higher likelihood that all particles within a cluster align in the same direction, resulting in a more uniform color within the cluster. This indicates that the particles have

a reduced tendency to rotate, leading to more coherent movement in a single direction. Consequently, the system achieves a highly ordered state, which is reflected in Fig. 5(c), where the  $\Phi$  reaches its maximum when  $v_0$  is at its highest value under low  $\Omega$  conditions.

As  $\Omega$  increases, the bias in particle orientation becomes stronger. This causes particles to rotate in different directions within a mixed state, resulting in the formation of distinct clusters containing both types of particles. In this mixed state, some clusters are dominated by particles with positive chirality, causing them to rotate clockwise (*CW*), while others are dominated by particles with negative chirality, leading them to rotate anti-clockwise (*ACW*) Fig. 5(c). However, these clusters are not perfectly ordered due to the mixed nature of the particles. As particles continuously join or leave the clusters, they do not rotate in a fixed radius, leading to frequent collisions between the mixed clusters. This behavior increases the overall randomness and disorder within the system, resulting in a sudden decrease in the  $\Phi$  value, marking a significant change. This behavior is shown by particles when  $v_0 \geq 0.07$ . At lower values of  $v_0$ , there is no sudden decrease in the  $\Phi$ ; instead, it decreases slowly and becomes approximately constant at large  $\Omega$ , indicating that the particles are moving very slowly and there is no collision between particle clusters. The mechanism of collision is shown in the zoomed snapshot of the particles' position with the orientation shown by arrows Fig. 5(c).

However, the particles eventually become fully phase-separated at higher  $v_0 (\geq 0.1)$  and increasing  $\Omega$ . At high velocities, a second maxima of  $\Phi$  is observed at  $\Omega$  around 0.1. Beyond this point, as  $\Omega$  increases further, the  $\Phi$  gradually decreases and stabilizes at an approximately constant value for a given  $v_0$ . Notably, the first maximum of the  $\Lambda(\mathcal{L})$  and the second maximum of the  $\Phi$  occur at the same value of  $\Omega$  for a particular velocity, signifying the appearance of macroscopic phase separated state with global rotation of particles within their clusters in the system.

## B. Dynamic of the system

Till now we discussed the characteristics of the system in terms of steady state in terms of ordering and density clusters for different activity and chirality. Now we will explore the dynamics of two types of particles in the system. We define the *Mean Square displacement (MSD)*  $\langle \Delta r^2 \rangle(t) = \frac{1}{N} \langle \sum_{i=1}^N |\mathbf{r}_i(t+t_0) - \mathbf{r}_i(t_0)|^2 \rangle$ , where  $\mathbf{r}_i(t)$  is the position of the  $i^{\text{th}}$  particle at time  $t$ ,  $t_0$  represents the reference time of the measurement. Here,  $\langle \dots \rangle$  indicates averaging over different values of  $t_0$  in

the steady state trajectory. In general,  $MSD$  follows a power-law dependence on  $t$ .  $\langle \Delta r^2 \rangle \sim t^\alpha$ , where the exponent  $\alpha = 1$  corresponds to diffusive motion,  $\alpha < 1$  to sub-diffusive motion, and  $\alpha > 1$  to super-diffusive motion, whereas for ballistic motion one has  $\alpha = 2$ . In

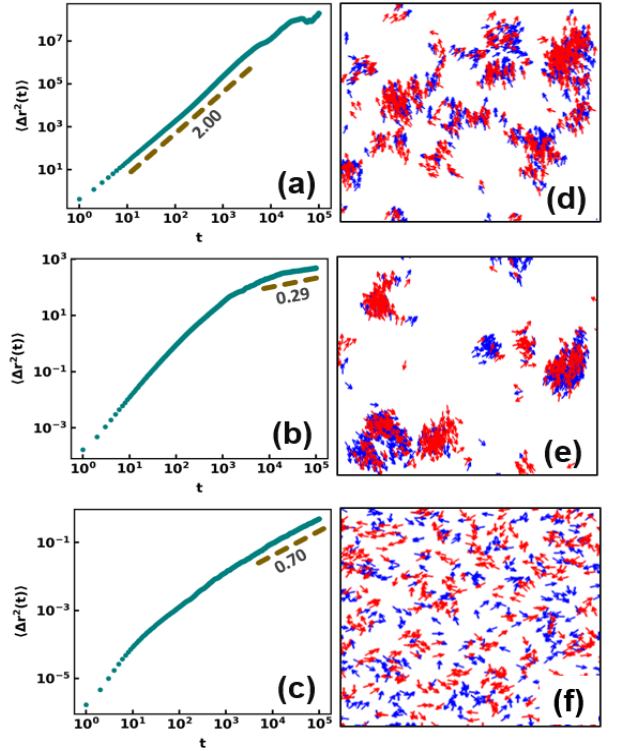


FIG. 6. (color online) (a – c)  $MSD \langle \Delta r^2(t) \rangle$  vs  $t$  plots for the parameters where we find mixing of two types of particles and (d – f) show the snapshots for the same parameters as for (a – c) respectively. The arrows in the snapshots represent the orientation of particles and colors have the same meaning as in Fig. 2(I). (a, d), (b, e), and (c, f) are for the set of parameters ( $v = 0.5, \Omega = 0.01$ ), ( $v = 0.01, \Omega = 0.05$ ) and ( $v = 0.001, \Omega = 0.5$ ).

Fig. 6(a-c) we again show the snapshots of the system for three different combinations of activity and chirality  $(v_0, \Omega) = (0.5, 0.01), (0.01, 0.05)$  and  $(0.001, 0.5)$  respectively. The three cases are chosen as follows: (a) When the trajectory of the particle is a nearly straight line (Fig. 2(I-II)(d) 3(d)). This case shows mixed flocking behavior, as seen by the ballistic nature of  $MSD$  in Fig. 6(a). However, in the end, the  $MSD$  shows saturation due to finite chirality in the system. This clearly explains the enhanced global order parameter  $\Phi$  and small  $PSOP$  for this set of parameters. In Fig. 6(e), we show the snapshot for  $v_0 = 0.01$  and  $\Omega = 0.05$ , where chirality starts to dominate and particles start moving in a small radius circle. Since the  $r_0 < R$ , the particles get a chance to mix and rotate in small clusters. The  $MSD$  shows the trapped motion at late times due to the rotational dynamic as shown in Fig. 6(b). Now as



we decrease  $v_0 = 0.001$  and increase  $\Omega = 0.5$  as shown in the snapshot in Fig. 6(f), chirality is dominant and particles mainly rotate about their axis without interacting with their neighbors. Hence, the system remains in homogeneous mixed phases with a very small magnitude of  $MSD$  in comparison to Fig. 6(b). The dynamics of the particle are very different for the two cases Figs. 6(b) and (c). In Fig. 6(b), when both activity and chirality have moderate values but activity dominates, particles can form mixed oriented clusters with a rotational tendency, leading to a very small  $MSD$  exponent  $\alpha \ll 1$ . On the other hand, for Fig. 6(c), when activity is very small and chirality is dominating, particles mainly rotate about their own axis with small random displacement from their mean position, resulting in a small magnitude of  $MSD$  and subdiffusive dynamics in the system

### C. Phase diagram

We have analyzed the steady-state features of the system with respect to activity and chirality, and we drew the phase diagram in the plane of activity  $v_0$  and chirality  $\Omega$  as shown in Fig. 7. The colors in each symbol represent the magnitude of  $PSOP$  and the different symbols are for four different phases found in the system based on the relative activity and chirality. We have already discussed the detailed characteristics of the system with respect to these different phases. Now based on their characteristics, here we name them and summarise. For very small chirality ( $\Omega \leq 0.01$ ) and across the entire range of activity, the particles exist in a mixed state with small correlation length and  $PSOP$  and flock in a common direction with moderate to large values of  $GOP$ , we refer to this phase as the mixed flocking phase ( $MFP$ ) and shown by the circles in Fig. 7. When the activity is small ( $v_0 < 0.001$ ) and there is finite chirality, the particles rotate about their axis and both types of particles remain mixed, resulting in small values of  $GOP$ ,  $PSOP$ , and  $\mathcal{L}$ . Such phase is shown by the pentagons in Fig. 7 and we named this phase and homogeneous rotating phase ( $HRP$ ). We have observed interesting phases emerging when activity and chirality compete. When the ratio  $r_0 < 1$ , the two types of particles get phase separated in small clusters, and both  $PSOP$  and  $GOP$  remain at moderate values. We define this phase as the microscopic phase separated phase ( $MiPS$ ), marked by triangles in Fig. 7. On the other hand, when the ratio is larger than  $R$ , macroscopic clusters of different types of particles are formed, and both  $PSOP$  and  $\mathcal{L}$  are large. This phase is named the macroscopic phase separated phase ( $MaPS$ ) and is represented by diamonds in Fig. 7. In the phase diagram, we have also shown the line with  $r_0 = R = 1$ . We can see that a simple mean field

argument of the radius of the trajectory of particles can mimic the macroscopic phase separation in the system. Except for very small  $\Omega = 0.01$  and  $v_0$ .

Till now we have discussed the steady properties of dif-

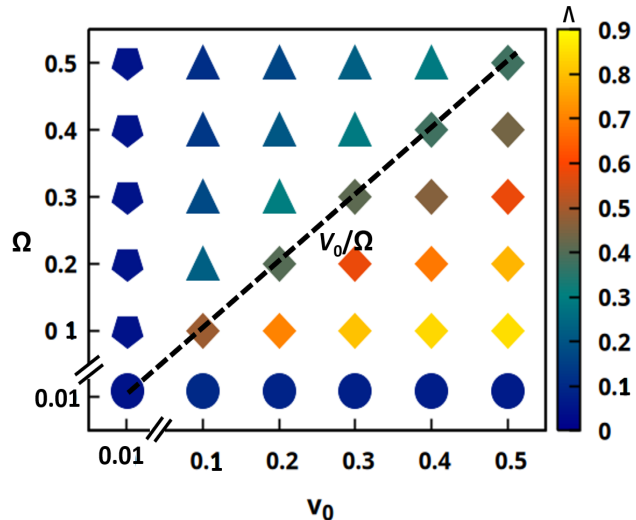


FIG. 7. (color online) Phase Diagram for different phases in  $(\Omega, v_0)$  plane. The circle shows the mixed flocking ( $MFP$ ), the pentagon shows the homogeneous rotating ( $HRP$ ), the triangle shows the microscopic phase separated ( $MiPS$ ), and the diamond shows the macroscopic phase separated ( $MaPS$ ). The color bar shows the magnitude of the  $PSOP$   $\Lambda$ . The black dotted line shows the  $\frac{v_0}{\Omega} = 1 = R$  line.

ferent phases. The macroscopic phase separated rotating phase ( $MaPS$ ) is the most interesting phase, where the two types of particles start to rotate in different clusters. Now we ask the question, what is the kinetics of the ( $MaPS$ ), when we start from the initial random disordered and mixed configuration?

### D. Kinetics of $MaPS$ phase

To understand the kinetics, we first observe the system's time evolution. In Fig.8 we show the snapshot of the local density difference  $\Delta\rho(\mathbf{r})$  at four different times  $t = 2^2, 2^6, 2^{10}$  and  $2^{16}$  for  $(v_0, \Omega) = ((0.1, 0.06), (0.3, 0.10), (0.5, 0.17))$ . The choice of parameters is only those combinations of activity and chirality where the  $PSOP$  and  $\mathcal{L}$  shows the maxima in Fig. 5(a-b). With time the phase separation among the two types of particles increases as can be seen by the appearance of bright spots in the last two columns of Fig. 8. Also, the size of colored regions increases with time. Further, we show the plot of the two-point correlation function of local density difference as defined previously in subsection III A. In Fig. 8(a-d) we show the plot of

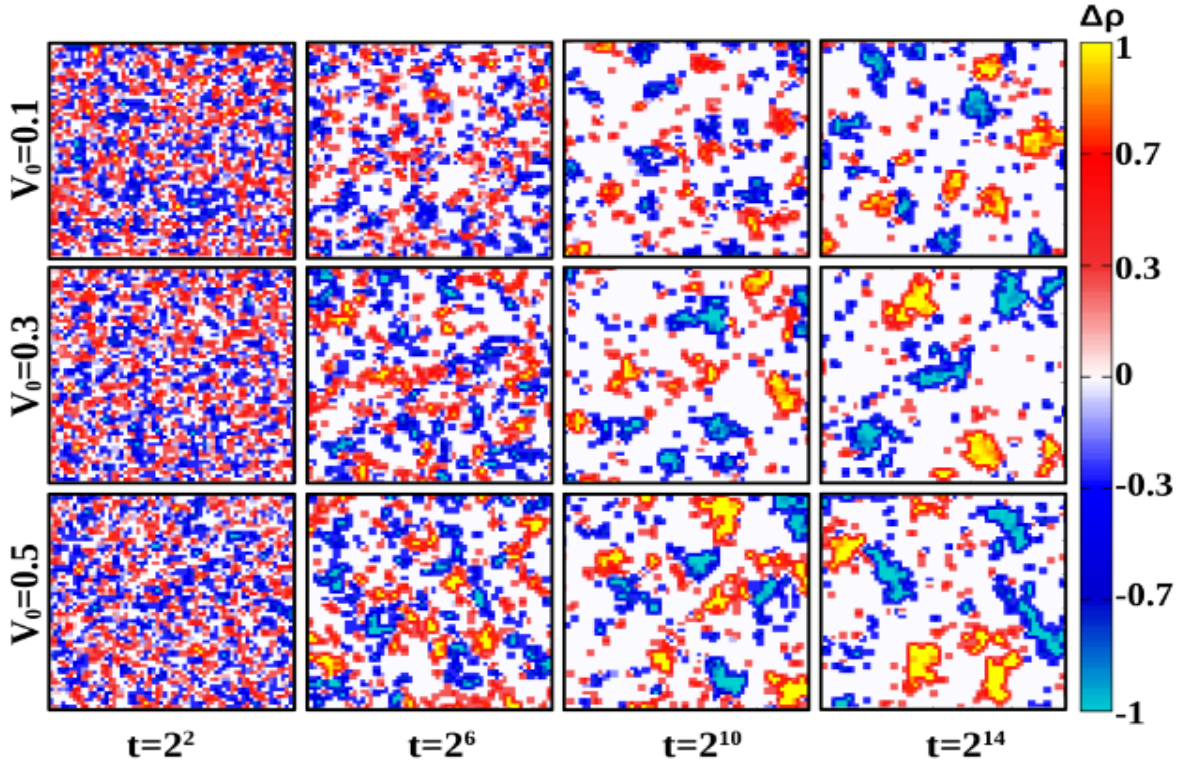


FIG. 8. (color online) Shows the time-dependent density difference  $\Delta\rho$  snapshots for different  $v_0$  and  $\Omega$  as  $(v_0, \Omega) = (0.1, 0.06), (0.3, 0.10), (0.5, 0.17)$  for  $t = 2^2, 2^6, 2^{10}$  and  $2^{16}$  and colour palette is same as in Fig.2(II).

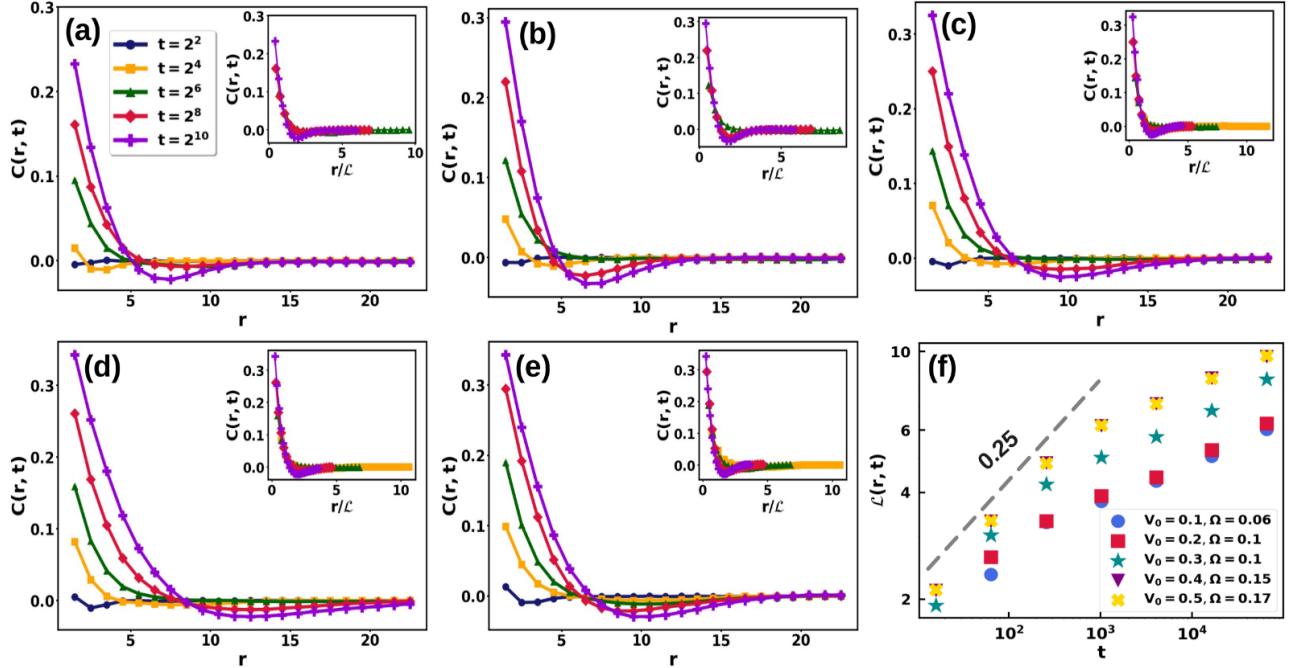


FIG. 9. (a)  $v_0 = 0.1$ , (b)  $v_0 = 0.2$ , (c)  $v_0 = 0.3$  and (d)  $v_0 = 0.4$  and (e)  $v_0 = 0.5$  is two-point correlation function  $C(r, t)$  vs.  $r$  at different times. *Insets*: the scaled  $C(r, t)$  vs scaled distance  $r/L$  for all five cases. (f) Plot of correlation length  $\mathcal{L}$  vs.  $t$  in the growing stage on log – log scale for different  $(v_0, \Omega)$  values.

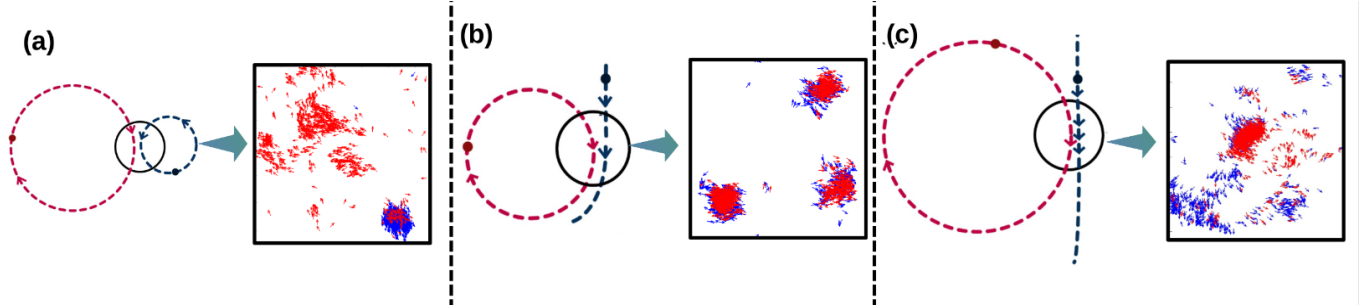


FIG. 10. (a) Cartoon of the trajectories of two particles for the asymmetric combinations of chirality. The color code and keys are the same as for Fig. 4. The snapshots on the right side of each panel show a part of the system for the same set of parameters. The keys of the snapshots are the same as for Fig. 6. (a – c) is for the set of parameters  $(v_0, \Omega^+, \Omega^-) = (0.5, 0.1, -0.3), (0.5, 0.1, 0)$  and  $(0.3, 0.1, 0)$  respectively.

$C(r, t)$  for four different combinations of  $(v_0, \Omega)$  the same for which the snapshots are shown in Fig. 8. With time correlation increases and further we calculated the correlation length  $\mathcal{L}(v_0, \Omega, t)$ . In the insets of Fig. 9(a-e) we show the scaled correlation function with scaled distance  $r/\mathcal{L}$  for five different times  $t = 2^2, 2^4, 2^6, 2^8, 2^{10}$ . The collapse of data for the scaled plots will represent the dynamic scaling in the system. Fig. 9(f) shows the variation of correlation length  $\mathcal{L}(v_0, \Omega, t)$  vs. time  $t$  for different combinations of  $(v_0, \Omega)$ . For all the cases, initially,  $\mathcal{L}$  grows with time with a power  $t^\gamma$ , with  $\gamma \sim 0.25$ , and at late times the growth of  $\mathcal{L}(v_0, \Omega, t)$  slows as the system approaches the steady state.

### E. Assymmetric mixture

Till now our focus was on the symmetric mixture of two types of chiral particles. Now we look for a case, where the magnitude of chirality of two types of particle, differ from each other. Hence we call it asymmetric mixture. In this case, again 50% of the particles exhibit clockwise (*CW*) chirality, while the remaining 50% exhibit anticlockwise (*ACW*) chirality, but the particles' chirality magnitudes are not equal, indicating that the orientation of the two types of particles is not exactly opposite to each other. We will discuss the three combinations of chirality and activity. (i) As shown in Fig. 10, *ACW*-chiral particles ( $\Omega^- = 0.3$ ) exhibit higher chirality compared to *CW*-chiral particles ( $\Omega^+ = 0.1$ ). In this case, chiral particle trajectories are a mixture of *Case-II* and *Case-III* as shown in Fig.4(b, c), and previously discussed in subsection III A. Due to their smaller curvature, blue (*ACW*) particles spend more time in the interaction range than red (*CW*) particles with larger curvature.

Consequently, particles with *-ve* chirality form one tight cluster and rotate due to their chirality, while *+ve* chiral

particles rotate in a dispersed manner in the system, as shown in the snapshot in Fig.10(a). The two other cases are (ii) when the one type particle is achiral  $\Omega^- = 0$  and  $\Omega^+ = 0.1$  and  $v_0 = 0.3$  for both types of particles. In Fig.10(b) we show the trajectory of two particles and the system snapshot at some fixed time in the steady state. In this scenario when activity is  $v_0 = 0.3$ , both types of particles form the mixed cluster and the mixture shows the chiral behavior. This happens because if the hopping step of particles is smaller than the  $R$  then particles have a higher tendency to remain within the interaction range for some time and get a chance to interact with the mixture. Also curvature of chiral particles is larger resulting in them following the circular trajectory of the chiral particles, and the non-chiral (blue) particles rotate due to the chirality of the *+ve* chiral particles as shown in the snapshot of Fig.10(b). However for the third case (c) when  $v_0 = 0.5$ , now the step size of particles is increased and this leads to the non-chiral particles leaving the surroundings of chiral particles very soon and they escape from the cluster of chiral particles as shown in Fig. 10(c).

## IV. DISCUSSION

We comprehensively studied a mixture of two types of chiral active particles. Most of our focus was on the symmetric mixture, where the two types of particles have the same magnitude of chirality but different signs. One type of particle rotates clockwise (*CW*) and the other type rotates counterclockwise (*ACW*). We used the activity  $v_0$  and the magnitude of chirality  $\Omega$  as the two control parameters in our model. The density of both types of particles was kept the same in the system. The magnitude  $\Omega$  measures the rotational nature of particles as well as the difference between the two types of particles. For small  $\Omega$ , the difference in chirality between the two types

of particles is small, causing them to remain in a mixed phase and move together in the same direction, Hence the system is found to be a mixed flocking phase (*MFP*). For small activity and finite chirality, chirality dominates and the particles remain mixed, rotating about their axis without much translational motion. This phase is named the homogeneous rotating phase (*HRP*). Interestingly, the system exhibits macroscopic phase separation and the rotating phase when activity and chirality are comparable. The phase separation in the system can be explained by defining the ratio  $r_0 = \frac{v_0}{\Omega}$ , such that when the ratio is larger than the interaction range, particles get phase separated in macroscopic clusters. Each cluster rotates globally in one direction. The chirality of the majority of particles in the cluster decides the direction of rotation. Further when the ratio  $r_0$  is smaller than the interaction range, then the two types of particles get phase separated in microscopic clusters. The clusters have the same tendency as found in macroscopic rotating clusters. The above two phases are named macroscopic phase separated (*MaPS*) and microscopic phase separated (*MiPS*) respectively. We also studied the kinetics of phase separation for the *MaPS*. We observed that the correlation length grows algebraically with time, with a growth exponent similar to the usual growth law for active systems [44, 46], and the system exhibits good dynamic scaling for large activities  $v_0$ . Although the system shows the four different phases concerning activity and chirality and interesting dynamic patterns, we discussed the explanation of the four phases in detail with

the help of simple mean field understanding using the radius of the particle trajectory and the interaction radius.

Furthermore, we explored asymmetric mixtures for a few combinations of activity and chirality, where the symmetric mixture system exhibits macroscopic phase-separated rotating clusters. We considered two cases where the chirality of one type of particle is smaller than the other, and two different activities are chosen,  $v_0 = 0.3$  and  $0.5$ . We found two different phases: mixed rotating and rotating flocking phase, respectively.

Our study provides a deep understanding of different phases for the mixture of chiral particles. The different phases we observed here can be useful to understand the patterns and dynamics observed in chiral active particles. The present study is limited to the point particles. It is interesting to explore the behavior of the system, where particles have finite size and shape which will make it closer to the many natural systems.

### Acknowledgement

The support and the resources provided by PARAM Shivay Facility under the National Supercomputing Mission, Government of India at the Indian Institute of Technology, Varanasi, are gratefully acknowledged by all authors. SM thanks S S Manna for useful discussions. SM thanks DST-SERB India, ECR/2017/000659, CRG/2021/006945, and MTR/2021/000438 for financial support, DK acknowledge the UGC India for financial support. DK and SM thank the Centre for Computing and Information Services at IIT(BHU), Varanasi.

- 
- [1] D. J. Sumpter, *Collective animal behavior* (Princeton University Press, 2010).
- [2] T. Vicsek and A. Zafeiris, *Physics reports* **517**, 71 (2012).
- [3] M. C. Marchetti, J.-F. Joanny, S. Ramaswamy, T. B. Liverpool, J. Prost, M. Rao, and R. A. Simha, *Reviews of modern physics* **85**, 1143 (2013).
- [4] I. Lavi, R. Alert, J.-F. Joanny, and J. Casademunt, *arXiv preprint arXiv:2407.15149* (2024).
- [5] S. Shankar, A. Souslov, M. J. Bowick, M. C. Marchetti, and V. Vitelli, *Nature Reviews Physics* **4**, 380 (2022).
- [6] C. Bechinger, R. Di Leonardo, H. Löwen, C. Reichhardt, G. Volpe, and G. Volpe, *Reviews of modern physics* **88**, 045006 (2016).
- [7] A. Cavagna, D. Conti, C. Creato, L. Del Castello, I. Giardina, T. S. Grigera, S. Melillo, L. Parisi, and M. Viale, *Nature Physics* **13**, 914 (2017).
- [8] A. J. Ward, D. J. Sumpter, I. D. Couzin, P. J. Hart, and J. Krause, *Proceedings of the National Academy of Sciences* **105**, 6948 (2008).
- [9] M. Ballerini, N. Cabibbo, R. Candelier, A. Cavagna, E. Cisbani, I. Giardina, V. Lecomte, A. Orlandi, G. Parisi, A. Procaccini, *et al.*, *Proceedings of the national academy of sciences* **105**, 1232 (2008).
- [10] A. Cavagna and I. Giardina, *Annu. Rev. Condens. Matter Phys.* **5**, 183 (2014).
- [11] N. Kumar, H. Soni, S. Ramaswamy, and A. Sood, *Nature communications* **5**, 4688 (2014).
- [12] T. Vicsek, A. Czirók, E. Ben-Jacob, I. Cohen, and O. Shochet, *Physical review letters* **75**, 1226 (1995).
- [13] F. Jülicher, A. Ajdari, and J. Prost, *Reviews of Modern Physics* **69**, 1269 (1997).
- [14] A. Najafi and R. Golestanian, *Physical Review E—Statistical, Nonlinear, and Soft Matter Physics* **69**, 062901 (2004).
- [15] M. Ebrahimian, M. Yekehzare, and M. R. Ejtehadi, *Physical Review E* **92**, 063035 (2015).
- [16] R. R. Bennett and R. Golestanian, *Physical review letters* **110**, 148102 (2013).
- [17] A. Chamolly, T. Ishikawa, and E. Lauga, *New Journal of Physics* **19**, 115001 (2017).
- [18] J. Zhang, B. A. Grzybowski, and S. Granick, *Langmuir* **33**, 6964 (2017).



- [19] H. Löwen, The European Physical Journal Special Topics **225**, 2319 (2016).
- [20] B. Friedrich, The European Physical Journal Special Topics **225**, 2353 (2016).
- [21] W. R. DiLuzio, L. Turner, M. Mayer, P. Garstecki, D. B. Weibel, H. C. Berg, and G. M. Whitesides, Nature **435**, 1271 (2005).
- [22] H. C. Berg and L. Turner, Biophysical Journal **58**, 919 (1990).
- [23] E. Lauga, W. R. DiLuzio, G. M. Whitesides, and H. A. Stone, Biophysical journal **90**, 400 (2006).
- [24] I. H. Riedel, K. Kruse, and J. Howard, Science **309**, 300 (2005).
- [25] J. Elgeti, R. G. Winkler, and G. Gompper, Reports on progress in physics **78**, 056601 (2015).
- [26] F. Kümmel, B. Ten Hagen, R. Wittkowski, I. Buttinoni, R. Eichhorn, G. Volpe, H. Löwen, and C. Bechinger, Physical review letters **110**, 198302 (2013).
- [27] K. Ērglis, Q. Wen, V. Ose, A. Zeltins, A. Sharipo, P. A. Janmey, and A. Čēbers, Biophysical journal **93**, 1402 (2007).
- [28] A. Čēbers, Journal of Magnetism and Magnetic Materials **323**, 279 (2011).
- [29] R. M. Harshey, Annual Reviews in Microbiology **57**, 249 (2003).
- [30] A. Sokolov, I. S. Aranson, J. O. Kessler, and R. E. Goldstein, Physical review letters **98**, 158102 (2007).
- [31] M. F. Copeland and D. B. Weibel, Soft matter **5**, 1174 (2009).
- [32] S. Chatterjee, M. Mangeat, C.-U. Woo, H. Rieger, and J. D. Noh, Physical Review E **107**, 024607 (2023).
- [33] L. J. Schumacher, P. K. Maini, and R. E. Baker, Cell systems **5**, 119 (2017).
- [34] J. W. Jolles, A. J. King, and S. S. Killen, Trends in ecology & evolution **35**, 278 (2020).
- [35] S. Peled, S. D. Ryan, S. Heidenreich, M. Bär, G. Ariel, and A. Be'Er, Physical Review E **103**, 032413 (2021).
- [36] S. Benisty, E. Ben-Jacob, G. Ariel, and A. Be'er, Physical review letters **114**, 018105 (2015).
- [37] W. Zuo and Y. Wu, Proceedings of the National Academy of Sciences **117**, 4693 (2020).
- [38] M. Deforet, C. Carmona-Fontaine, K. S. Korolev, and J. B. Xavier, The American Naturalist **194**, 291 (2019).
- [39] D. Levis, I. Pagonabarraga, and B. Liebchen, Physical Review Research **1**, 023026 (2019).
- [40] B. Liebchen and D. Levis, Physical review letters **119**, 058002 (2017).
- [41] D. Levis and B. Liebchen, Physical Review E **100**, 012406 (2019).
- [42] B. Ventejou, H. Chaté, R. Montagne, and X.-q. Shi, Physical review letters **127**, 238001 (2021).
- [43] J. Mecke, J. O. Nketsiah, R. Li, and Y. Gao, National Science Open **3**, 20230086 (2024).
- [44] S. Pattanayak, S. Mishra, and S. Puri, Soft Materials **19**, 286 (2021).
- [45] S. Pattanayak, J. P. Singh, M. Kumar, and S. Mishra, Physical Review E **101**, 052602 (2020).
- [46] G. S. Redner, M. F. Hagan, and A. Baskaran, Phys. Rev. Lett. **110**, 055701 (2013).